Sharp volumetric billboard based characterization and modeling of complex 3D Ni/Al high energy ball milled composites

Dewen Yushu[a], Sangmin Lee[b], Karel Matouš[a,b,1,*]

[a] Department of Aerospace and Mechanical Engineering, University of Notre Dame, Notre Dame, IN 46556, USA
[b] Center for Shock Wave-processing of Advanced Reactive Materials, University of Notre Dame, Notre Dame, IN 46556, USA

A B S T R A C T

We present an innovative image-based modeling technique, based on Google Earth like algorithms, to effectively resolve intricate material morphology and address the computational complexity associated with heterogeneous materials. This sharp volumetric billboard algorithm stems from a volumetric billboard method, a multi-resolution modeling strategy in computer graphics. In this work, we enhance volumetric billboards through a sharpening filter to reconstruct the statistical information of heterogeneous systems. A hierarchy of microstructures is created for high energy ball milled Ni/Al composites. We analyze the first- and second-order statistics of microstructures, and characterize both macro- and micro-mechanical material responses. Furthermore, we conduct a convergence study of the associated computational results. The statistical and mechanical robustness of data compression is demonstrated through the corresponding error analysis.

1. Introduction

Heterogeneous materials are abundant in nature as well as in synthetic applications. Typical examples include polycrystalline materials, polymer blends, porous media, metal alloys, etc. Predicting the behavior of heterogeneous materials, whether mechanical (Matouš et al., 2008; Lee et al., 2011; Kulkarni et al., 2009; Meyers et al., 2006; Fu et al., 2008), thermal (Gillman and Matouš, 2014; Gillman et al., 2015; Srinivasan et al., 2009; Hartl and Lagoudas, 2008), electrical (Seto, 1975; Montal and Mueller, 1972; Allaoui et al., 2002) or otherwise, has been a long standing endeavor. These material properties strongly depend on the size, shape and spatial distribution of each phase. One such complex material system is a high energy ball milled (HEBM) composite. HEBM composites play an important role in pyrotechnics, propellants, shock synthesis, etc. (Manukyan et al., 2015; Zhang, 2004). The structure of HEBM materials is highly inhomogeneous, tortuous and stochastic, with varying size scales (see Fig. 1). Due to the complexity of the internal morphology, robust characterization and modeling techniques are needed when analyzing HEBM composites and other similar material structures.

Predictive microstructual modeling hinges on the structural information acquired from imaging techniques. In the recent decades, the development of three dimensional (3D) high resolution imaging, either destructive (Shuck et al., 2016; Uchic et al., 2006), or non-destructive (Gillman et al., 2013; Collins et al., 2008; Lee et al., 2009; Arns et al., 2002), has enabled measurements of the size, shape and connectivity of microstructural features on micro, nano or even atomic scales. The 3D analysis pushes the frontier of imaging techniques by reducing the sampling bias associated with two dimensional (2D) analysis and enabling a valid description of the internal 3D structural characteristics as a whole. This includes devices and methods such as the electron atom probe (Blavette et al., 1993; Gerstl et al., 2004), tomographic transmission electron microscopy (Frank, 1992; Midgley and Weyland, 2003), synchrotron-based X-Ray diffraction (Schmidt et al., 2004; Larson et al., 2002), focused ion beam (FIB), and sectioning electron microscopy (SEM) (Shuck et al., 2016; Uchic et al., 2006), just to name a few.

Currently, microstructural modeling is undergoing a revolutionary change corresponding to the improvements of material processing and imaging techniques. For example, to capture structural details reflected in the high-resolution images, studies are carried out using voxel based modeling (Huang and Li, 2013; Lewis and Geltmacher, 2006; Huang et al., 2015), where one voxel in the digital image corresponds to one finite element (FE). To this end, the voxel based models are extremely expensive, considering the significant amount of voxels in the high resolution images. To re-
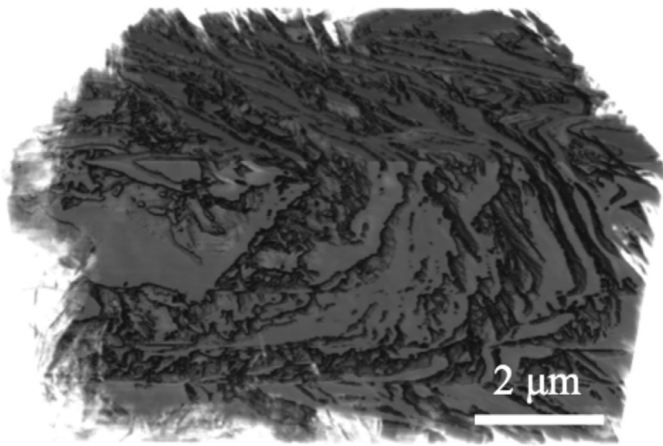
Fig. 1. Material morphology of a HEBM Ni/Al composite in 3D from the FIB/SEM method (Shuck et al., 2016). Only the Al phase is displayed.

lieve the computational burden, model reduction is required. One of the traditional approaches is to choose a representative computational domain (Huang and Li, 2013). This leads to the challenge of balancing between the micro-structural size and the resolution of structural features. Another approach is to group and/or merge the voxels (Lewis and Geltmacher, 2006; Huang et al., 2015). This approach enables analysis on a larger physical domain with the same number of elements. However, the geometrical and physical implications of grouping voxels are usually ignored, which in turn weakens the reliability of associated numerical results.

Instead of manipulating the voxels directly, reconstruction methods utilize idealized shapes extracted from the digital images to construct a representative volume that describes the overall morphology (Gusev, 1997; Böhm et al., 2002). In volume reconstruction, many assume random fields and include artificially generated phases randomly distributed in space (Song et al., 2006; Man and van Mier, 2008; Drummond et al., 2005; Chawla et al., 2006). Others employ statistical correlation functions that are ascertained from digital images to quantify the shape and distribution of phases (Lee et al., 2009; Gillman et al., 2013; Klemm et al., 1997; Yeong and Torquato, 1998a). In general, reconstruction methods are well suited for analyzing heterogeneous materials when the morphology of at least one of the phases is regular and approaches idealized geometries such as spheres, ellipsoids, tetrahedrons, etc. However, structural assumptions and simplifications in this approach become unrealistic when modeling highly complex systems with extremely irregular morphologies, such as in Fig. 1. Furthermore, unlike voxel based methods, the computational cost and accuracy of reconstruction models rely largely on the subsequent meshing process, which can potentially introduce additional numerical errors (Huang et al., 2015). To this end, modeling extremely complex heterogeneous materials with high fidelity, while reducing the computational complexity of the underlying data, requires a novel approach.

Similar to our challenges in finding a balance between capturing realistic micro-structural details and reducing computational burdens, researchers studying computer graphics came across problems associated with accommodating complex geometries while maintaining real-time rendering rates. Much of the work has been done in recent decades to resolve this problem (Lorensen and Cline, 1987; Heckbert and Garland, 1994; Goswami et al., 2013; Rodríguez et al., 2013; Decaudin and Neyret, 2004; 2009; Lindstrom et al., 1996). For example, the volumetric billboard (VB) method (Decaudin and Neyret, 2009; 2004), an advanced 3D version of mipmaps (Williams, 1983; Tanner et al., 1998), which relies directly on the voxelization of objects

(Decaudin and Neyret, 2009) can avoid the potential anamorphic effects that are produced through the image processing. Moreover, the VB method introduces a hierarchy of image details, or level of details (LODs) (Luebke, 2003), and gives rise to a series of structures containing fewer and fewer geometrical primitives. This algorithm has been proven to be efficient in rendering trees, foliage, clouds, complex scenes, etc., and is used in a wide range of applications, such as Google Earth and countless modern computer games (Décoret et al., 2003; Behrendt et al., 2005). Although the VB method has provided a possibility of "lossless" data compression, current implementations mainly take visual effects into account. The effects of objects, either geometrical, statistical or physical, on material properties are yet to be analyzed.

In our work, we innovatively show the undesirable statistical effect of a traditional voxel-reduction method by computing correlation functions, which are fundamental for capturing the morphology of random materials. To reconstruct statistical properties, we establish an enhanced scheme, the sharp volumetric billboard (SVB). Here, one SVB step is composed of a down-sampling and a sharpening procedure, where a unique sharpening filter is designed to minimize the greyscale probability mass function error with local volume conservation. To demonstrate our approach, we utilize a fine LOD microstructure of HEBM Ni/Al composites from SEM/FIB (Shuck et al., 2016) to create a hierarchy of microstructures through the SVB scheme. Consistent high-order statistical properties are retained among SVB microstructures despite the large data compression ratios. To characterize mechanical properties, a parallel generalized finite element code, *PGFem3D*, is employed to compute mechanical responses for microstructures under tension-relaxation loading conditions using crystal plasticity constitutive equations (Matouš and Maniatty, 2004; 2009).

The paper is organized as follows. In Section 2, we discuss the sharp volumetric billboard theory and numerical algorithms. Examples of SVB microstructures are shown for HEBM Ni/Al FIB images. In Section 3, we talk about statistical descriptors and statistical characterization of SVB microstructures. Section 4 is dedicated to the constitutive theory of crystal plasticity. In Section 5, we present numerical results for SVB microstructures undergoing a tension-relaxation loading process. Finally, in Section 6, we draw conclusions and discuss potential for future work.

2. Sharp volumetric billboard

In this section, we describe the SVB method. In order to create the SVB of a material body, we use an image set taken from imaging techniques (i.e., SEM/FIB method, see Fig. 1). We denote this image set as the finest level, or the 0th LOD. Mathematically, the nth LOD-SVB can be denoted by a three-dimensional container $^{n}\mathcal{V}_{ijk}$, where the left superscript is a LOD identifier. This container satisfies the Einstein notation rules and stores greyscale values associated with the digital images. The greyscale values are integers carrying the intensity information, which range between $0 - 255$ for 8-bit images, for instance. The indices of $^{n}\mathcal{V}_{ijk}$ satisfy $i \in [1, {}^{n}X], j \in [1, {}^{n}Y], k \in [1, {}^{n}Z]$, with

$$^{n}X = \left\lfloor \frac{^{0}X}{2^n} \right\rfloor, \quad ^{n}Y = \left\lfloor \frac{^{0}Y}{2^n} \right\rfloor, \quad ^{n}Z = \left\lfloor \frac{^{0}Z}{2^n} \right\rfloor, \quad (1)$$

where $\lfloor \cdot \rfloor$ is the round down operator. ^{0}X, ^{0}Y, ^{0}Z are the discrete data included in the finest image set along three directions in the cartesian coordinates. The fact that ^{n}X, ^{n}Y and ^{n}Z decrease as n increases is caused by the down-sampling procedure described in Section 2.1. Along with the decrease in the amount of data, the physical size represented by each data point (voxel) increases ac-
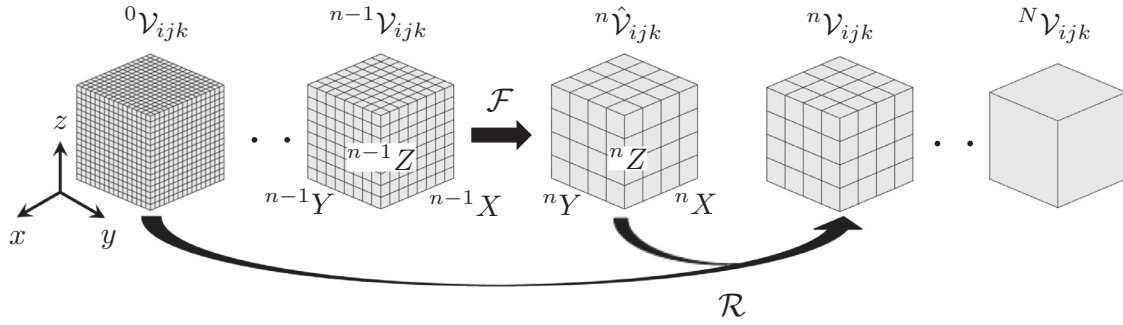
Fig. 2. Sharp volumetric billboard scheme.

cordingly

$$^{n}l_x = \frac{L_x}{^{n}X}, \quad ^{n}l_y = \frac{L_y}{^{n}Y}, \quad ^{n}l_z = \frac{L_z}{^{n}Z}, \tag{2}$$

where $^{n}l_x$, $^{n}l_y$, $^{n}l_z$ are the voxel dimensions of the nth LOD along the x, y and z directions. Here, L_x, L_y, L_z represent the physical size of the image set along three directions. For the sake of simplicity, the nth LOD-SVB can be alternatively described by a spatial piecewise function

$$^{n}\mathcal{V}(x, y, z) = {^{n}\mathcal{V}_{mpq}}, \text{ with } m = \left\lceil \frac{x}{^{n}l_x} \right\rceil, \quad p = \left\lceil \frac{y}{^{n}l_y} \right\rceil, \quad q = \left\lceil \frac{z}{^{n}l_z} \right\rceil, \tag{3}$$

where $\lceil \cdot \rceil$ is the round up operator, $x \in [0, L_x]$, $y \in [0, L_y]$, $z \in [0, L_z]$. In what follows, $^{n}\mathcal{V}(x, y, z)$ and $^{n}\mathcal{V}_{ijk}$ identically refer to the nth LOD-SVB.

The SVB sequence is shown in Fig. 2. Starting from the finest LOD, $^{0}\mathcal{V}_{ijk}$ is passed through a down-sampling filter $\mathcal{F}$ and a sharpening filter $\mathcal{R}$ sequentially to create the next LOD-SVB, $^{1}\mathcal{V}_{ijk}$. This procedure is repeated until the coarsest LOD, say $^{N}\mathcal{V}_{ijk}$, is obtained. The $^{n}\hat{\mathcal{V}}_{ijk}$ symbol is employed to differentiate the intermediate step before the sharpening filter is applied (see Fig. 2). Details about the two filters are described in Sections 2.1 and 2.2, respectively.

2.1. Down-sampling filter $\mathcal{F}$

The filter $\mathcal{F}$ is a linear filter for image down-sampling. It is constructed from three directional back-to-front α-blending filters (Porter and Duff, 1984; Mammen, 1989). As shown in Fig. 2, this filter inputs a finer LOD ($^{n-1}\mathcal{V}_{ijk}$) and outputs a coarser LOD ($^{n}\hat{\mathcal{V}}_{ijk}$). Every sampled greyscale value in $^{n}\hat{\mathcal{V}}_{ijk}$ is the round-down weighted average of $^{n-1}\mathcal{V}(x, y, z)$ in a rectangular region of dimension $^{n}l_x \times {^{n}l_y} \times {^{n}l_z}$. The formulation of $\mathcal{F}$ reads

$$^{n}\hat{\mathcal{V}}_{ijk} = \mathcal{F}(^{n-1}\mathcal{V}(x, y, z))$$
$$= \left\lfloor \int_{\Delta v} {^{n-1}T(x, y, z) \cdot {^{n-1}\mathcal{V}(x, y, z)} \, \mathrm{d}x\mathrm{d}y\mathrm{d}z} \right\rfloor, \tag{4}$$

where $\Delta v = [(i - 1) \cdot {^{n}l_x}, i \cdot {^{n}l_x}] \times [(j - 1) \cdot {^{n}l_y}, j \cdot {^{n}l_y}] \times [(k - 1) \cdot {^{n}l_z}, k \cdot {^{n}l_z}]$ is the physical volume of one voxel in the down-sampled image with index (ijk) and $^{n-1}T(x, y, z)$ is an user defined spatial piecewise weighting function for the $(n - 1)$th LOD-SVB in Δv. This function satisfies

$$^{n-1}T(x, y, z) = {^{n-1}T_{mpq}} \geq 0 \quad \text{and} \quad \int_{\Delta v} {^{n-1}T(x, y, z)} \, \mathrm{d}x\mathrm{d}y\mathrm{d}z = 1, \tag{5}$$

where $m = \lceil \frac{x}{^{n-1}l_x} \rceil$, $p = \lceil \frac{y}{^{n-1}l_y} \rceil$, $q = \lceil \frac{z}{^{n-1}l_z} \rceil$. The weighting characterizes the transparency of the image primitives in Δv. For example, for any $\tilde{v}$ in Δv, $\int_{\tilde{v}} {^{n-1}T(x, y, z)} \, \mathrm{d}\tilde{v} = 0$ represents 100%

transparency, $\int_{\tilde{v}} {^{n-1}T(x, y, z)} \, \mathrm{d}\tilde{v} = 1$ represents total opacity, and a value in between represents translucency. In our case, we choose $^{n-1}T(x, y, z)$ to be a constant, because none of the image primitives dominate in the nth LOD. This gives

$$^{n-1}T(x, y, z) = \frac{1}{^{n}l_x{^{n}l_y}{^{n}l_z}}. \tag{6}$$

The filter $\mathcal{F}$ is commonly used for voxel merging and grouping when down-sampling images during image processing (Lin and Dong, 2006; Russ and Woods, 1995). However, as a low pass filter, it tends to corrupt the high frequency component of the image, and thus blurs the geometrical edges and discontinuities. As a result, it usually produces images that are not sharp (Jain, 1989). After down-sampling the image several times using $\mathcal{F}$, the image suffers from severe high frequency information loss, which results in corresponding material behavior bias. Therefore, we propose a novel sharp filter to reconstruct the material information. This filter, represented by $\mathcal{R}$, is described next.

2.2. Sharp filter $\mathcal{R}$

The filter $\mathcal{R}$ is created to reconstruct the original phase contrast after image down-sampling. The creation of this filter is under the premise that the down-sampling filter $\mathcal{F}$ smoothes the material density distributions (as seen later in Section 2.3), which results in relatively large changes in the material behavior. To resolve limitations introduced by the filter $\mathcal{F}$, while taking advantage of the down-sampled image, we propose to restore the lost material contrast through another filtering process. As can be seen from Fig. 2, $\mathcal{R}$ uses information from the original image, $^{0}\mathcal{V}_{ijk}$, reads in the nth LOD down sampled image, $^{n}\hat{\mathcal{V}}_{ijk}$, reconstructs the phase contrast and produces SVB, $^{n}\mathcal{V}_{ijk}$. More specifically, $\mathcal{R}$ utilizes the probability mass function (PMF) from the original image to guide the amount of greyscale value interchange. Moreover, it locally limits the altering range of data in every voxel to keep the original geometrical features. To this end, we also refer to $\mathcal{R}$ as the global-local voxel-matching filter, since it uses the global information from $^{0}\mathcal{V}_{ijk}$ and performs the local operations on $^{n}\hat{\mathcal{V}}_{ijk} \rightarrow {^{n}\mathcal{V}_{ijk}}$.

To mathematically describe the functionality of the filter $\mathcal{R}$, we first define the greyscale PMF for $^{n}\hat{\mathcal{V}}_{ijk}$, which reads

$$^{n}\hat{\mathcal{P}}(\rho) = \frac{\sum_{\tilde{z}=1}^{^{n}Z} \sum_{\tilde{y}=1}^{^{n}Y} \sum_{\tilde{x}=1}^{^{n}X} I(^{n}\hat{\mathcal{V}}_{\tilde{x}\tilde{y}\tilde{z}}, \rho)}{^{n}X \cdot {^{n}Y} \cdot {^{n}Z}}, \tag{7}$$

where the hat (ˆ) and the left-superscript are consistent with the image set identifier, $\rho \in \mathbb{Z}^1$ is the greyscale value that is related to the material density ($\rho \in [0, 255]$ for 8-bit greyscale images), and I is a piecewise function defined as

$$I(^{n}\hat{\mathcal{V}}_{\tilde{x}\tilde{y}\tilde{z}}, \rho) = \begin{cases} 1 & \text{if } {^{n}\hat{\mathcal{V}}_{\tilde{x}\tilde{y}\tilde{z}}} = \rho, \\ 0 & \text{otherwise.} \end{cases} \tag{8}$$

Based on Eq. (7), the contrast difference between $^n\hat{\mathcal{V}}_{ijk}$ and $^0\mathcal{V}_{ijk}$ can be quantified by the L^1-norm

$$E = \sum_\rho \left| {}^n\hat{\mathcal{P}}(\rho) - {}^0\mathcal{P}(\rho) \right|. \tag{9}$$

Here, the sum is over all discrete greyscale values.

To reconstruct the original contrast, we propose to use E as an objective function. However, simply minimizing E can lead to multiple admissible microstructures, many of which are undesirable because they often suffer from phase distortions. This problem is caused by the spatially unrestricted greyscale value interchange. To resolve this problem and prevent the voxel switching between the material phases, we constrain the range of manipulated greyscale values for every voxel as follows,

$$\left| {}^n\mathcal{V}_{\tilde{x}\tilde{y}\tilde{z}} - {}^n\hat{\mathcal{V}}_{\tilde{x}\tilde{y}\tilde{z}} \right| \le d, \tag{10}$$

$$\forall \quad \tilde{x} \in [1, {}^nX_n], \ \tilde{y} \in [1, {}^nY_n], \ \tilde{z} \in [1, {}^nZ_n], \tag{10}$$

where $d > 0$ is a prescribed maximum range of the greyscale value interchange for every voxel. The choice of d depends on the phase contrast (the lower the contrast, the smaller d). For one given microstructure, we find its nth LOD-SVB microstructure by minimizing Eq. (9) under the constraint in Eq. (10).

We note that the optimization problems that minimize differences of morpholgical functions between real and synthetic microstructures (e.g. Eq. (9) with constraint Eq. (10)) are common in computational material science (Lee et al., 2009; Matouš et al., 2000; 2017; Kumar et al., 2006; Yeong and Torquato, 1998b; Kumar et al., 2008). In particular, researchers formulate various types of objective functions, including statistical correlation functions (Lee et al., 2009; Kumar et al., 2006; Yeong and Torquato, 1998b; Kumar et al., 2008), intensity functions (Matouš et al., 2000) and power spectral density functions (Povirk, 1995). Despite the type of the objective function, solving the optimization problem is generally difficult, because many local minima exist. Moreover, successfully traversing all possible realizations and solving for the global minimum can be computationally demanding. Algorithms used in this regard range from genetic algorithms (Matouš et al., 2000; Kumar et al., 2008), simulated annealing (Kumar et al., 2006; Yeong and Torquato, 1998b) to hybrid global-local minimizers (Lee et al., 2009; Povirk, 1995).

In this work, we propose a novel numerical algorithm that approximates the minimum by matching the greyscale value PMF through a fast sweeping strategy with local volume preservation (LVP). The sweeping procedure rules out unacceptable solutions by driving E close to its minimum while imposing a strong constraint by implicitly setting $d = 1$. To realize LVP, we assume conformity of the voxels: the greyscale value of one voxel is more likely to be increased if it is surrounded by voxels with the higher greyscale values, and vice versa. After accepting this assumption, we weight every voxel in $^n\hat{\mathcal{V}}_{ijk}$ by accounting for their corresponding neighboring voxels. Thus, we create image weights, $^n\hat{\mathcal{W}}_{ijk}$, for every $^n\hat{\mathcal{V}}_{ijk}$ by averaging the greyscale values of neighbor voxels in the weighting region (WR). The WR of one voxel is the set that includes the voxel itself and every voxel that contacts it,

$$\text{WR}(^n\hat{\mathcal{V}}_{ijk}) = \{ {}^n\hat{\mathcal{V}}_{\tilde{x}\tilde{y}\tilde{z}} : i-1 < \tilde{x} < i+1, j-1 < \tilde{y} < j+1,$$
$$k-1 < \tilde{z} < k+1 \}, \tag{11}$$

where $\tilde{x}, \tilde{y}$ and $\tilde{z}$ also satisfy the indexing constraint for $^n\hat{\mathcal{V}}_{ijk}$. The image weight, $^n\hat{\mathcal{W}}_{ijk}$, is the average of the greyscale values in WR,

$$^n\hat{\mathcal{W}}_{ijk} = \frac{\sum_{{}^n\hat{\mathcal{V}}_{\tilde{x}\tilde{y}\tilde{z}} \in \text{WR}(^n\hat{\mathcal{V}}_{ijk})} {}^n\hat{\mathcal{V}}_{\tilde{x}\tilde{y}\tilde{z}}}{\text{card}[\text{WR}(^n\hat{\mathcal{V}}_{ijk})]}, \tag{12}$$

where the sum is over all of the discrete values in WR and card(·) gives the cardinality of a set. Fig. 3 shows a specific optimization
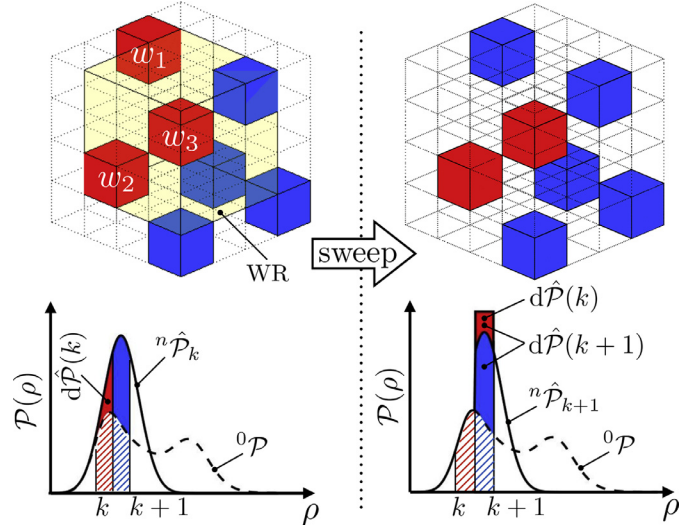

Fig. 3. Filter $\mathcal{R}$ strategy. Red blocks represent the voxels that have the greyscale value $\rho = k$ and blue blocks represent the voxels that have the greyscale value $\rho = k+1$. Here, $^n\hat{\mathcal{P}}_k$ and $^n\hat{\mathcal{P}}_{k+1}$ denote PMFs before and after sweeping, respectively. The image above shows a specific case when $d\hat{\mathcal{P}}(k) > 0$ and the weight value, $w_1 > w_2 > w_3$. The WR for the voxel where the weight value equals w_3 is shown in light yellow. (For interpretation of the references to colour in this figure legend, the reader is referred to the web version of this article.)

step of $\rho = k \rightarrow \rho = k+1$. As shown in Fig. 3, to match the original PMF, one of the three voxels that has the greyscale value $\rho = k$ needs to be assigned to $\rho = k+1$. As a result, the voxel which has the highest weight is chosen, because it resides in a region where the digitized microstructure has high greyscale values. In this way, the volume of each phase is approximately preserved locally in the neighboring region of each voxel. An implementation of the filter $\mathcal{R}$ for creating $^n\mathcal{V}_{ijk}$ is provided in Algorithm 1.

Algorithm 1 – Filter $\mathcal{R}$.

1: Derive $^0\mathcal{P}$ and $^n\hat{\mathcal{P}}$ for the finest image $^0\mathcal{V}_{ijk}$ and the nth LOD intermediate image $^n\hat{\mathcal{V}}_{ijk}$ from Eq. (7).

2: Create the image weight, $^n\hat{\mathcal{W}}_{ijk}$, by averaging the neighbor elements in the WR for every voxel in $^n\hat{\mathcal{V}}_{ijk}$.

3: Initialize $\rho = 0$.

4: Determine the greyscale value PMF difference, $d\hat{\mathcal{P}}(\rho) = {}^n\hat{\mathcal{P}}(\rho) - {}^0\mathcal{P}(\rho)$, and derive the number of voxels to be redistributed to (when $d\hat{\mathcal{P}}(\rho) > 0$) or restored from (when $d\hat{\mathcal{P}}(\rho) < 0$) the aggregate of elements with the greyscale value $\rho + 1$.

5: **if** $d\hat{\mathcal{P}}(\rho) > 0$ **then**

6:     Get the weight values (WV) of the elements that have the same greyscale value ρ from the image weight $^n\hat{\mathcal{W}}_{ijk}$ and choose those elements that have the largest weights.

7:     Set the greyscale value of the chosen elements to be $\rho + 1$.

8: **if** $d\hat{\mathcal{P}}(\rho) < 0$ **then**

9:     Get the WV of the elements that have the same greyscale value $\rho + 1$ from the image weight $^n\hat{\mathcal{W}}_{ijk}$ and choose those elements that have the smallest weights.

10:     Set the greyscale value of the chosen elements to be ρ.

11: **if** $d\hat{\mathcal{P}}(\rho) = 0$ **then** Go to next step.

12: Update $\rho \leftarrow \rho + 1$, and repeat step 4 - 11 until $\rho = 255$ (for 8-bit images).

Table 1
Model parameters for the different LOD.

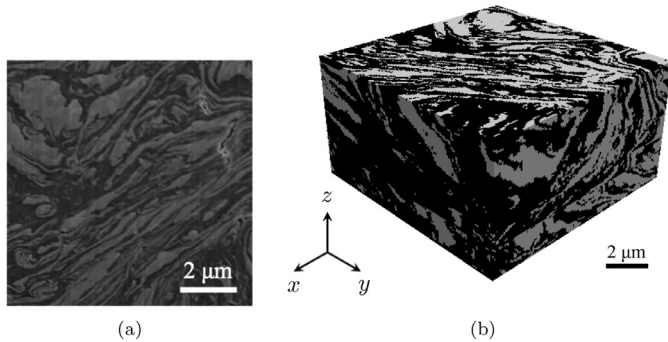| LOD	Physical size [μm^3]	Number of voxels	Voxel size [nm^3]	Compression Ratio
0th	349.4	1.035e+8	$15 \times 15 \times 15$	–
1st	349.4	1.294e+7	$30 \times 30 \times 30$	8
2nd	349.4	1.617e+6	$60 \times 60 \times 60$	64
3rd	349.4	2.022e+5	$120 \times 120 \times 120$	512
4th	349.4	2.462e+4	$240 \times 240 \times 246$	4204

Fig. 4. The original Ni/Al image. (a) One greyscale 2D image extracted from the original image set (Shuck et al., 2016), where the Ni phase is brighter, the Al phase is darker. (b) Binary 3D microstructure, where grey identifies the Ni phase, black identifies the Al phase.

2.3. SVB of Ni/Al composites.

To verify our SVB algorithm, we apply the SVB scheme to HEBM Ni/Al composites. The HEBM technique takes the single-phase Ni (fcc) and Al (fcc) powders and combines them into a Ni/Al particle with nanoscale geometric features that contain both phases with oxide-free boundaries. The HEBM is done in a planetary mill under an inert atmosphere. The milling conditions are set to prevent chemical reactions and atomic mixing. Therefore, the mixture con-

tains no secondary phases (i.e., only Ni and Al are present). More details about the HEBM procedure can be found in Manukyan et al. (2015); Shuck et al. (2016); Fecht et al. (1990). Due to the HEBM process, the resultant Ni/Al composites acquire a highly stochastic and tortuous internal structure, which is suitable for testing the robustness of our SVB algorithm.

As a demonstration, we create a series of SVB microstructures of HEBM Ni/Al composites up to the 4th LOD. The number of LODs acceptable for an accurate analysis depends on several factors, i.e., the material contrast, complexity of the microstructure, etc. The model parameters of each SVB with varying LOD are listed in Table 1. The HEBM Ni/Al image data obtained by Shuck et al. (2016) is shown in Fig. 4. The Ni/Al nanocomposite is produced from an equiatomic (~2:3 volumetric) mixture of Ni and Al through HEBM. An image stack is first collected through the FIB/SEM approach and then reconstructed after the shear correction, contrast normalization and alignment, which results in an image stack with 15nm resolution. We choose from this image stack a volume of interest with 312 image slices, each clipped to 576×576 pixels. This corresponds to a physical domain of $L_x = 8.64\mu m$, $L_y = 8.64\mu m$, $L_z = 4.68\mu m$ along the x, y and z directions, respectively.

Slices extracted at the same location along the z direction in each of the SVB, and the averaged (AVG) microstructures are shown in Fig. 5. The AVG microstructures are created by solely applying the filter $\mathcal{F}$ on the same image set, as is traditionally done in computational materials science (Lewis and Geltmacher, 2006; Pyle et al., 2013; Qidwai et al., 2009). The morphology of the Ni/Al composite is highly complex due to the HEBM procedure. However, the SVB series still captures this morphology well, even after a data compression to 0.024% of the original data for the 4th LOD. It should be noted that a dark zone appears in the higher LOD-SVB (Fig. 5a– d) to match the discontinuous features, such as pores and impurities in the composite (marked by a box in Fig. 5). In comparison with the SVB series, the coarser LOD-AVG microstructures become less clear and cannot resolve the small discontinuous features (compare Fig. 5d and h).
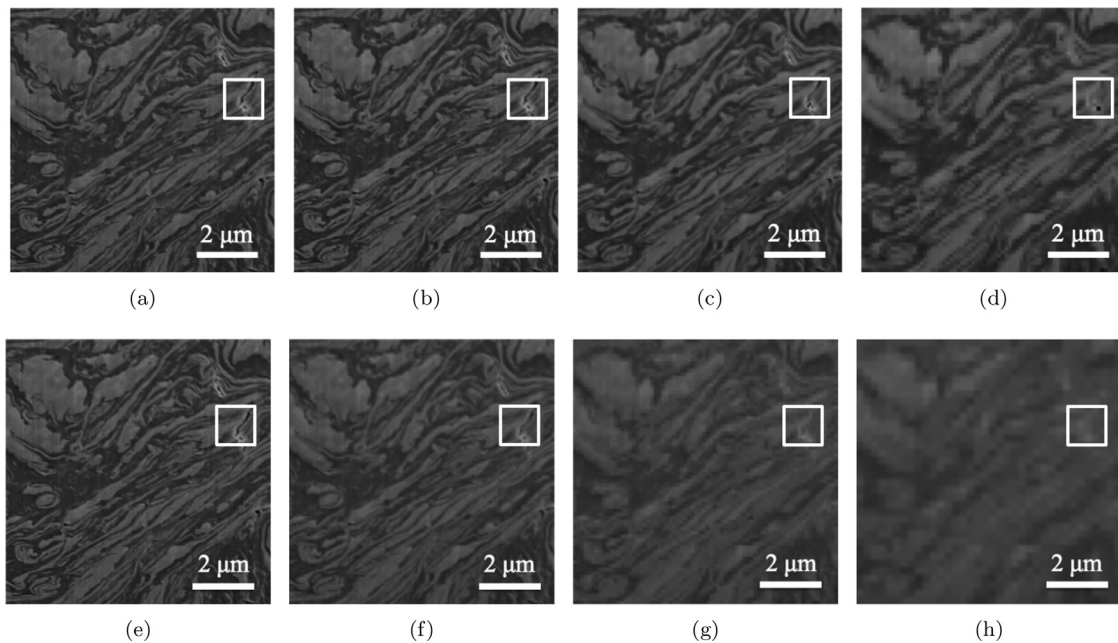

Fig. 5. One slice extracted from the SVB (a-d) and AVG (e-h) microstructures up to the 4th LOD. All microstructures are of the same physical size, 3.494e+2 μm^3. The resolution of the image is different: (a, e) $288 \times 288 \times (156)$, (b, f) $144 \times 144 \times (78)$, (c, g) $72 \times 72 \times (39)$, and (d, h) $36 \times 36 \times (19)$ in voxels, respectively. The last number in brackets represents the third dimension (number of slices). The boxed area shows an example of a structure with a sharp gradient of the greyscale values (e.g., a void).
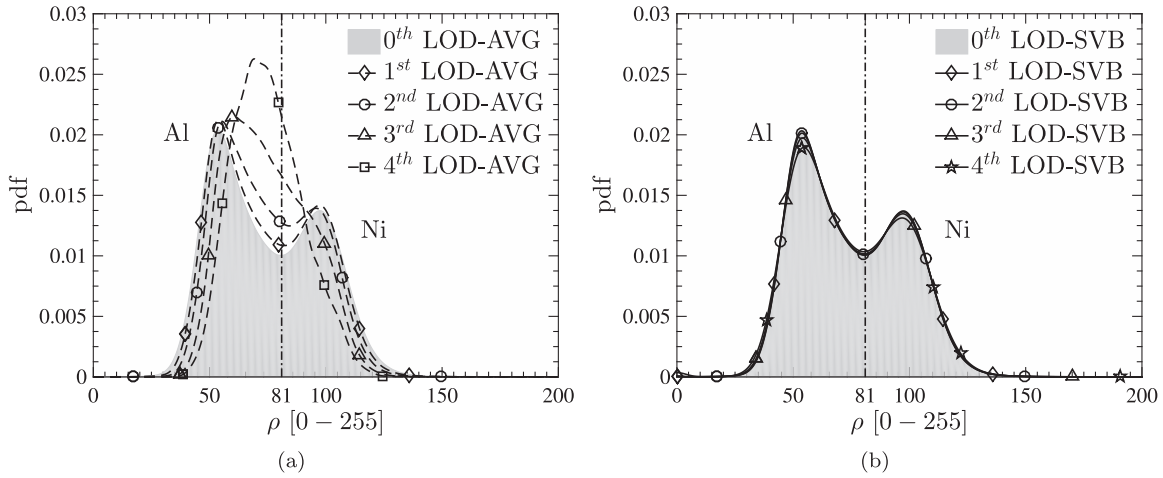
Fig. 6. The probability density function of the greyscale values up to the 4th LOD: (a) AVG, and (b) SVB. The vertical dot-dash line marks the threshold greyscale value.

To verify the SVB method, we compute the probability density function (pdf) of the greyscale values for SVB microstructures up to the 4th LOD (Fig. 6b). The pdfs are computed by fitting the greyscale value PMFs with the nonparametric kernel distributions. The shaded area represents the pdf from the finest LOD, which is used as a reference. The shape is approximately a union of two Gaussian distributions, with the left peak identifying the Al phase, and the right representing the Ni phase. The pdfs of SVB microstructures trace the reference pdf, which indicates density preservation of each phase (the greyscale values can be related to the material density). Moreover, the invariance of the pdfs shows the robustness of the SVB scheme against the increasing LOD (decreasing voxel/element amount).

As a comparison, we also compute the greyscale value pdfs of AVG microstructures up to the 4th LOD (Fig. 6a). The pdf of the 0th LOD is shaded again as the reference. The resulting pdfs of the AVG microstructures drift further away with the increase of LOD, which indicates the high sensitivity of the AVG microstructures to LOD change. Moreover, the pdf saddle is swallowed starting at the 3rd LOD, which renders the two phases indistinguishable, which is also reflected intuitively in Fig. 5g and h.

To separate the Ni and Al phases, we use Otsu's method (Otsu, 1975) to binarize the greyscale images. This method helps to find the optimum threshold greyscale value, which maximize the interphase variance. In our case, the threshold value for the 0th LOD image is $\rho = 81$ (the saddle value in Fig. 6a) and all images are segmented at the same greyscale value.

3. Statistical characterization

To characterize the geometrical effects of the SVB method, we utilize statistical descriptors. Specifically, we compute the one- and two-point probability functions. As described in Torquato (2002); Beran and Pytte (1968), the probability functions are derived using a phase indicator function at a material point $\boldsymbol{x}$ in a sample ω of an ensemble space Ω:

$$\mathcal{I}_a(\boldsymbol{x}; \omega) = \begin{cases} 1 & \text{if } \boldsymbol{x} \text{ in phase } a, \\ 0 & \text{otherwise.} \end{cases} \tag{13}$$

The ensemble is a collection of the material samples being considered. The ensemble average is given by

$$\overline{\mathcal{I}_a(\boldsymbol{x})} = \int_\omega \mathcal{I}_a(\boldsymbol{x}; \omega) \text{pdf}(\omega) \text{d}\omega, \tag{14}$$

where pdf(ω) is the probability density function of ω in Ω. Under the assumption of ergodicity, statistical homogeneity and isotropy,

the ensemble average can be replaced by the infinite volume average and the probability functions are translation and direction invariant (Torquato, 2002; Beran and Pytte, 1968; Torquato, 2013). To this end, the one-point probability function $\mathcal{C}_a$ reduces to the volume fraction. The two-point probability function, $\mathcal{S}_{a,b}(\boldsymbol{x}_1, \boldsymbol{x}_2)$, which represents the probability of finding phases a and b at points $\boldsymbol{x}_1$ and $\boldsymbol{x}_2$ simultaneously, depends on the distance r only (Torquato, 2002):

$$\mathcal{S}_{a,b}(r = |\boldsymbol{x}_1 - \boldsymbol{x}_2|) = \overline{\mathcal{I}_a(\boldsymbol{x}_1) \mathcal{I}_b(\boldsymbol{x}_2)}$$
$$= \lim_{V \to \infty} \frac{1}{V} \int_V \mathcal{I}_a(\boldsymbol{x}_1 - \boldsymbol{l}) \mathcal{I}_b(\boldsymbol{x}_2 - \boldsymbol{l}) \text{d}V. \tag{15}$$

Here, $\boldsymbol{l}$ is a translation vector and V is the volume of the domain.

The one- and two-point probability functions are computed using the parallel statistical sampling code, *Stat3D* (Lee et al., 2009; Gillman et al., 2013). In order to conveniently express the probability functions with respect to LODs, we let $^n\mathcal{C}_a$ denote the one-point probability function of the phase a at the nth LOD, and $^n\mathcal{S}_{a,b}$ represents the two-point probability function of the phase a and b at the nth LOD. To measure the change of one point probability functions, we define the volume fraction error of the phase a at the nth LOD as:

$$\epsilon\left(^i\mathcal{C}_a\right) = \frac{\left|^0\mathcal{C}_a - ^n\mathcal{C}_a\right|}{^0\mathcal{C}_a} \times 100\%. \tag{16}$$

The resulting one point probability function of the Al phase, $^n\mathcal{C}_{Al}$, is shown in Fig. 7a. Solid and dotted lines represent the SVB and AVG microstructures, respectively. The $^n\mathcal{C}_{Al}$ of AVG microstructures increases as the LOD increases. On the other hand, the SVB preserves $^n\mathcal{C}_{Al}$ despite the LOD change. The associated errors, $\epsilon(^n\mathcal{C}_{Al})$, are shown in Fig. 7b. The one point probability error of SVB is constrained within 0.35% at the 4th LOD, while the error introduced by the AVG at the same LOD reaches 9.61%.

Fig. 8b shows the isotropic two point probability functions, $\mathcal{S}_{Al,Al}$ and $\mathcal{S}_{Ni,Al}$, for the SVB microstructures. The two-point probability functions from different LODs stay close to each other, although the error of the 4th LOD is observable when the sampling distance r is small. This is due to the higher sensitivity of the two-point probability functions to the local morphologies. Specifically, the increase of the LOD results in a larger volume represented by one data point (voxel). As a result, geometrical features that have dimensions smaller than one voxel are more inclined to vanish.

As a comparison, we present the isotropic two point probability functions for the AVG microstructures in Fig. 8a. In general, the two-point probability functions of the AVG deviate dramati-
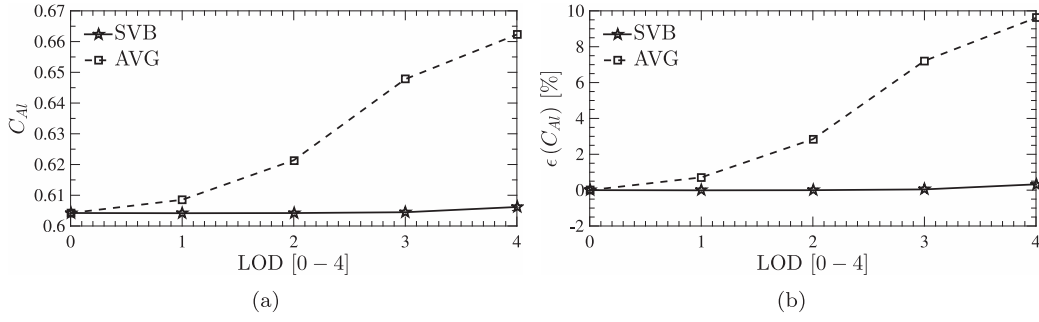
Fig. 7. One point probability function of the Al phase for the AVG and SVB: Change of (a) volume fraction ${}^n c_{Al}$, and (b) volume fraction error $\epsilon({}^n c_{Al})$ with respect to the LOD.
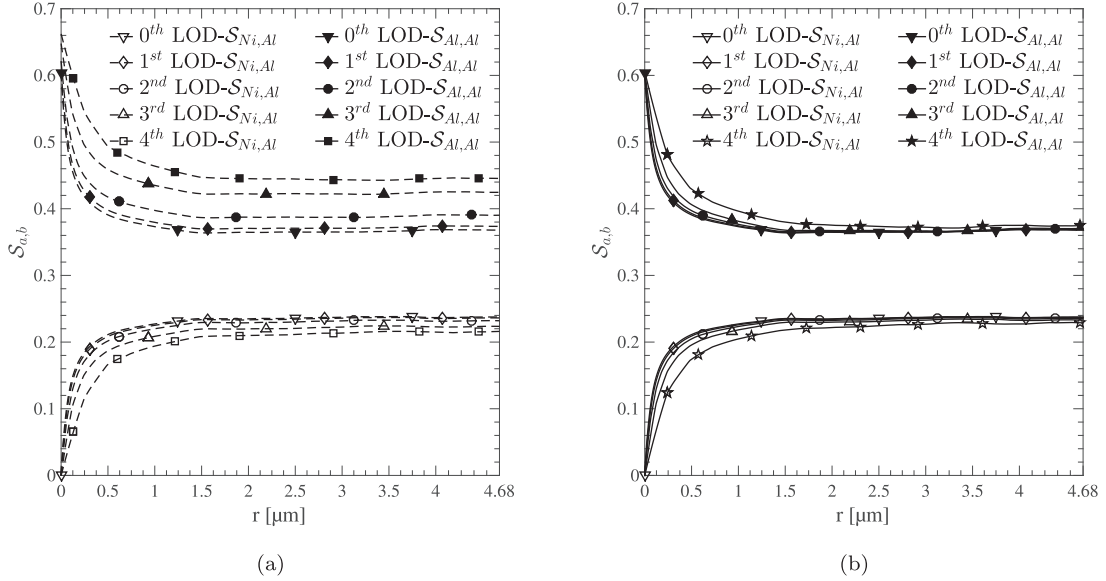

Fig. 8. The isotropic two-point probability functions of HEBM Ni/Al composites up to the 4th LOD: (a) AVG, (b) SVB.

cally from that of the finest LOD. Moreover, the AVG microstructures lose more accuracy as the higher LOD is reached.

4. Governing equations

As demonstrated in Sections 2 and 3, the SVB microstructures preserve both geometrical and statistical features with a high data-compression ratio. Next, we are interested in the mechanical response of the Ni/Al composite. In order to show the mechanical behavior, we utilize a finite strain model to solve the quasi-static equilibrium boundary value problem, which is governed by:

$$\begin{aligned}
\nabla \cdot \boldsymbol{P} + \boldsymbol{b} &= \boldsymbol{0} && \text{in } \Omega, \\
\boldsymbol{P} \cdot \boldsymbol{N} &= \bar{\boldsymbol{t}} && \text{on } \partial\Omega^t, \\
\boldsymbol{u} &= \bar{\boldsymbol{u}} && \text{on } \partial\Omega^u.
\end{aligned} \tag{17}$$

Here, $\boldsymbol{P}$ is the first Piola–Kirchhoff (P-K) stress tensor, $\boldsymbol{N}$ is the unit normal associated with $\partial\Omega^t$, $\boldsymbol{b}$ is the body force, $\bar{\boldsymbol{t}}$ is the traction applied on $\partial\Omega^t$, and $\bar{\boldsymbol{u}}$ is the applied displacement on $\partial\Omega^u$. Details of the numerical implementation using the mixed three-field finite element method is given in Matouš and Maniatty (2004).

4.1. Constitutive theory

Crystal-plasticity constitutive laws are used for numerical simulations (Matouš and Maniatty, 2004; 2009). The viscoplastic slip along a crystallographic slip plane is modelled assuming a power

law

$$\dot{\gamma}^\iota = \dot{\gamma}_0 \frac{\tau^\iota}{g^\iota} \left| \frac{\tau^\iota}{g^\iota} \right|^{1/\bar{m}-1}, \tag{18}$$

where $\bar{m}$ is a material rate sensitivity parameter, $\dot{\gamma}_0$ is a reference rate and g^ι is a resistence to the plastic slip (hardness) on a slip system ι. The resolved shear stress τ^ι is related to the second P-K stress $\boldsymbol{S}$

$$\tau^\iota = ({}^e\boldsymbol{C}\boldsymbol{S}) : \boldsymbol{P}^\iota, \tag{19}$$

where ${}^e\boldsymbol{C}$ is the elastic right Cauchy-Green deformation tensor and $\boldsymbol{P}^\iota$ denotes the Schmid tensor. To describe the evolution of the hardness, we adopt a uniform self and latent hardening. Thus, all slip systems start with the same hardness and harden together at the same rate. Therefore, the superscript ι can be dropped from the hardness, and the evolution equation yields

$$\dot{g} = G(\dot{\gamma}, g)\dot{\gamma} = G_0 \left(\frac{g_s - g}{g_s - g_0} \right) \dot{\gamma}, \tag{20}$$

where a hardening rate G_0 and an initial resolved shear strength g_0 are material parameters. Here, $\dot{\gamma}$ denotes the total shearing rate on all slip systems

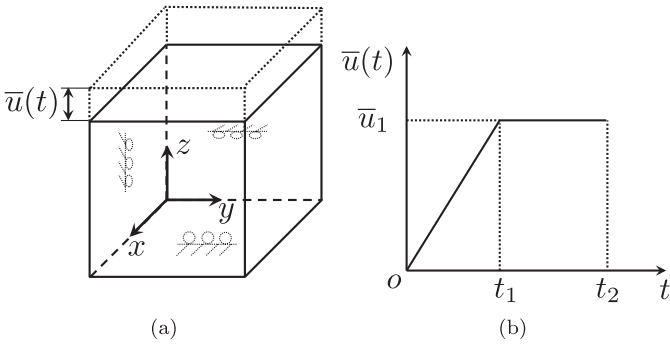$$\dot{\gamma} = \sum_{\iota=1}^{N_s} |\dot{\gamma}^\iota|, \tag{21}$$

Fig. 9. The tension-relaxation loading profile. (a) The schematic of the loading condition. (b) The displacement function $\bar{u}(t)$, where $t_1 = 119$ ms, $t_2 = 300$ ms, $\bar{u}_1 = 0.119\mu$m.

where N_s represents the total number of slip systems for a crystal. The saturation value of the hardness, g_s, is given by

$$g_s = g_{s_0} \left| \frac{\dot{\gamma}}{\dot{\gamma}_s} \right|^\omega, \tag{22}$$

where g_{s_0}, $\dot{\gamma}_s$ and ω are material parameters. Again, an efficient integration algorithm and numerical implementation are provided in Matouš and Maniatty (2004).

5. Numerical example

As an illustration of the SVB method, we simulate the mechanical response of HEBM Ni/Al composites utilizing the parallel generalized finite element code, *PGFem3D*, with crystal plasticity constitutive equations (Mosby and Matouš, 2015a; 2015b; 2016). In our work, two sets of simulations are performed. In the first set, we keep the identical texture for all microstructures (i.e., a single crystal representation) to avoid potential side-effects from the crystal orientation mapping among LODs. The associated results are presented in Sections 5.1 and 5.2. In the second set, we adopt random crystal orientations (i.e., a polycrystal representation) to simulate the real material texture. The corresponding results are included in Section 5.3.

In both cases, we compute the mechanical response of the 2nd to 4th LOD-SVB in order to analyze the effect of varying the LOD. Note that these LODs provide a series of microstructures, and thus, we investigate its convergent properties using the Richardson extrapolation (RE) in Sections 5.1 and 5.2. The SVB microstructures are created following the description in Section 2. For comparing and analyzing the influence of the SVB method on mechanical behaviors, we also simulate the response of the 4th LOD-AVG and the 4th LOD random (RND) microstructures. The 4th LOD-AVG is created from the same image set by solely applying the filter $\mathcal{F}$. We generate five 4th LOD-RND microstructures through random assignment of properties in each voxel while retaining the 4th LOD-SVB volume fraction.

The microstructures are subject to a tension-relaxation loading profile. The schematic of the loading history is shown in Fig. 9. We apply symmetric Dirichlet boundary conditions on the faces $x = 0$ (back), $y = 0$ (left) and $z = 0$ (bottom). The displacement $\bar{u}$ is applied along the $+z$ direction on the top surface, with specifics given in Fig. 9b. The value of maximum displacement $\bar{u}_1$ corresponds to the strain of 2.5% and t_1 is chosen so that the displacement rate along $+z$ direction becomes 10μm/s.

Structured finite element meshes with hexahedron elements are generated directly from the digital image stacks. The finest LOD numerically simulated in our work is the 2nd LOD. The 2nd LOD-SVB contains 1,617,408 brick elements, 1,660,975 nodes and 129,392,640 nonlinear crystal plasticity ODEs (see Section 4.1). The simulations are performed on $512 - 1024$ cores using C-SWARM cluster, LANL Mustang and LLNL CAB computing resources. Computing resources on the MIRA supercomputer at Argonne were also utilized. We assume the isotropic elastic material properties. The total number of slip systems for Ni and Al is $N_s = 12$. The material properties are listed in Table 2.

5.1. Macro-mechanical response

To examine the macro-mechanical (overall) behavior, we compare among all microstructures the average normal Cauchy stress along the $+z$ direction at the top surface, $\bar{\sigma}_{zz}$, defined as:

$$\bar{\sigma}_{zz} = \frac{1}{A} \int_A \sigma_{zz} dA. \tag{23}$$

Here, A is the undeformed area of the top surface. It should be noted that we employ the undeformed surface area, because we are in the small strain regime macroscopically. To quantify the error associated with the higher LOD microstructures, we utilize the following error

$$\epsilon(^n\bar{\sigma}_{zz}) = \frac{|^2\bar{\sigma}_{zz} - {}^n\bar{\sigma}_{zz}|}{\max|^2\bar{\sigma}_{zz}|}, \tag{24}$$

where the superscripts $n > 2$ are the LOD identifiers. The left superscript, 2 (i.e., $n = 2$), marks the finest LOD analyzed in our work.

The stress-time comparison among the SVB microstructure series is shown in Fig. 10a, which indicates very similar behavior of all three SVB microstructures. Note again that the Ni and Al phases are treated as single crystals in the initial configuration in this study. We select this orientation to limit the combined effects of morphology and texture. Fig. 10b shows the error introduced by the higher LOD-SVB microstructures. The error of $\bar{\sigma}_{zz}$ for the 4th LOD-SVB is controlled within 1.89% throughout the entire loading process, while the maximum error of the 3rd LOD-SVB is 0.83%.

To analyze the convergence rate of SVB microstructures, we use RE (Richardson, 1911; Richardson and Gaunt, 1927) on SVB computational results at two critical points, $\bar{\sigma}_{zz}(t_1)$ and $\bar{\sigma}_{zz}(t_2)$. This allows us to infer the error of the 2nd LOD-SVB microstructure with respect to the continuum description (0th LOD). We list the computational value $\bar{\sigma}_{zz}^C(t)$, the extrapolated value $\bar{\sigma}_{zz}^E(t)$, and the extrapolated relative error $\epsilon(\bar{\sigma}_{zz}^C(t))$ associated with the 2nd LOD-

Table 2
Viscoplastic properties of Ni and Al. Material properties of Al are from Matouš and Maniatty (2004). Material properties of Ni are from Turner et al. (2012). These material properties are typical and have been adopted in various studies (Choi et al., 2014; Bozek et al., 2008; Matouš and Maniatty, 2009). Moreover, the stress-strain response of each phase can be found in Matouš and Maniatty (2004); Pyle et al. (2013); Turner et al. (2012); Choi et al. (2014).

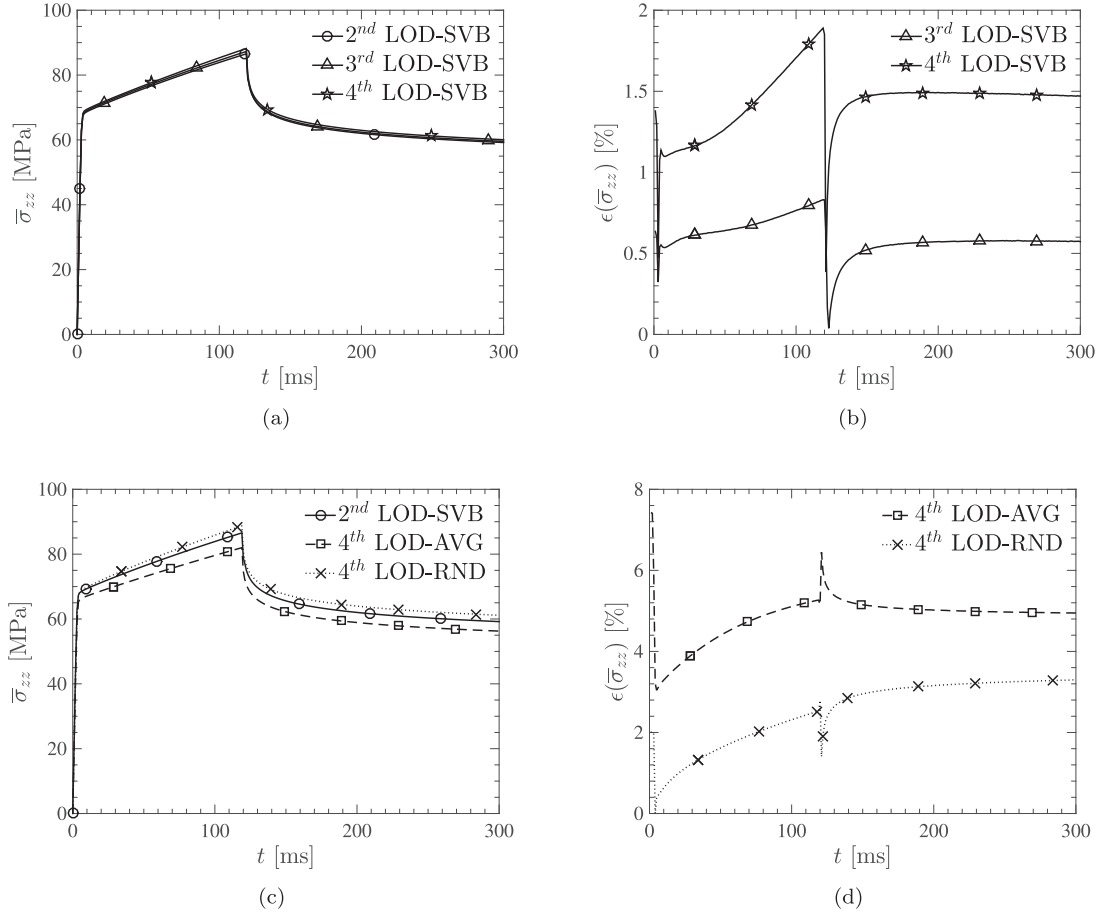| Material	E [GPa]	G [GPa]	$\bar{m}$	g_0 [GPa]	$\dot{\gamma}_0$ [s^{-1}]	G_0 [GPa]	g_{s_0} [GPa]	$\dot{\gamma}_s$ [s^{-1}]	ω
Ni	207	79.01	0.60	0.045	1.0	0.50	0.155	5.0e10	5.0e-4
Al	70	26.12	0.05	0.027	1.0	0.06	0.062	5.0e10	5.1e-6

Fig. 10. Average normal stress and associated error. (a) Average normal stress, $\bar{\sigma}_{zz}$, of the 2nd, 3rd, and 4th LOD-SVB microstructures. (b) Error for the 3rd and 4th LOD-SVB microstructures. (c) Average normal stress, $\bar{\sigma}_{zz}$, for the 2nd LOD-SVB, AVG, and RND. (d) Error for the AVG and RND.

Table 3
Richardson extrapolation results at the critical points $\bar{\sigma}_{zz}(t_1)$ and $\bar{\sigma}_{zz}(t_2)$.

RE point	$\bar{\sigma}_{zz}^C(t)$	$\bar{\sigma}_{zz}^E(t)$	$\epsilon(\bar{\sigma}_{zz}^C(t))$
t_1	86.56	86.35	0.2420%
t_2	59.19	58.94	0.4242%

SVB in Table 3. The extrapolated relative error is defined as

$$\epsilon(\bar{\sigma}_{zz}^C(t)) = \frac{|\bar{\sigma}_{zz}^E(t) - \bar{\sigma}_{zz}^C(t)|}{|\bar{\sigma}_{zz}^E(t)|}. \tag{25}$$

The extrapolated relative error for both points is less than 0.5%, which indicates that the computational results for the SVB microstructures quickly converge to the theoretical prediction.

For comparison, we show the computational result for AVG and RND microstructures together with the 2nd LOD-SVB result in Fig. 10c. Once again, the RND and AVG microstructures have the single crystal (Ni and Al) orientation in this study. The RND curve is the average of the aforementioned five microstructures (realizations). The coefficient of variation is CV($\bar{\sigma}_{zz}$) = 2.3%. Both AVG and RND microstructures introduce a noticeable discrepancy from the 2nd LOD throughout the whole loading process. The corresponding error is shown in Fig. 10d, which indicates that the error introduced by the AVG has exceeded 7.43% and the error of averaged five RND microstructures has reached 3.30%. We note that the trends between the AVG and RND responses in Fig. 10c and d depend on the particular microstructure.

5.2. Micro-mechanical response

To study the micro-mechanical behavior, we analyze the local stress field. Thus, we compute the distribution of the effective stress, σ_{eff}, associated with every element. The effective stress is defined as

$$\sigma_{\text{eff}} = \sqrt{\frac{3}{2}\boldsymbol{\sigma}' : \boldsymbol{\sigma}'}, \tag{26}$$

where $\boldsymbol{\sigma}'$ is the deviatoric part of the Cauchy stress.

To show the stress distribution, we display 3D plots of the effective stress at two critical time points, i.e., the maximum stress point t_1, and the relaxation point t_2, in Fig. 11. Both Fig. 11a and b show higher stress in the Ni phase compared to that of the Al phase, which is due to the higher stiffness of Ni (see Table 2). By comparing two stress fields, we observe the evolution of the local stress during the stress relaxation process.

To further quantify the local stress features, we compute the pdfs of the effective stress for all microstructures at the two critical loading points, t_1 and t_2. The pdfs are computed through fitting the nonparametric kernel distributions to σ_{eff} associated with all elements. To measure the error of the pdfs, we introduce the normalized error $\epsilon(^n\text{pdf})$, which measures the difference between two distributions:

$$\epsilon(^n\text{pdf}) = \frac{|{}^2\text{pdf} - {}^n\text{pdf}|}{\max|{}^2\text{pdf}|}. \tag{27}$$

Fig. 12 shows the pdfs and the associated errors of the 2nd to 4th LOD-SVB. The pdfs at both loading points can capture the
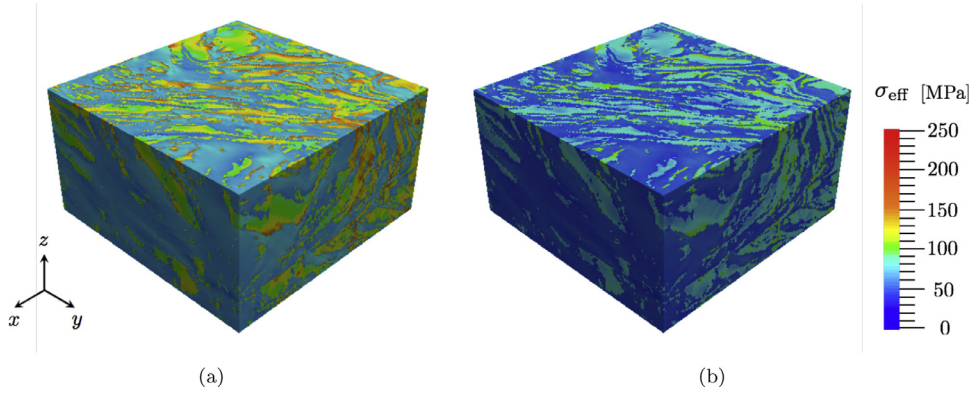
Fig. 11. Effective stress field associated with the 2nd LOD-SVB. (a) Stress at the maximum strain. (b) Stress at the end of relaxation.
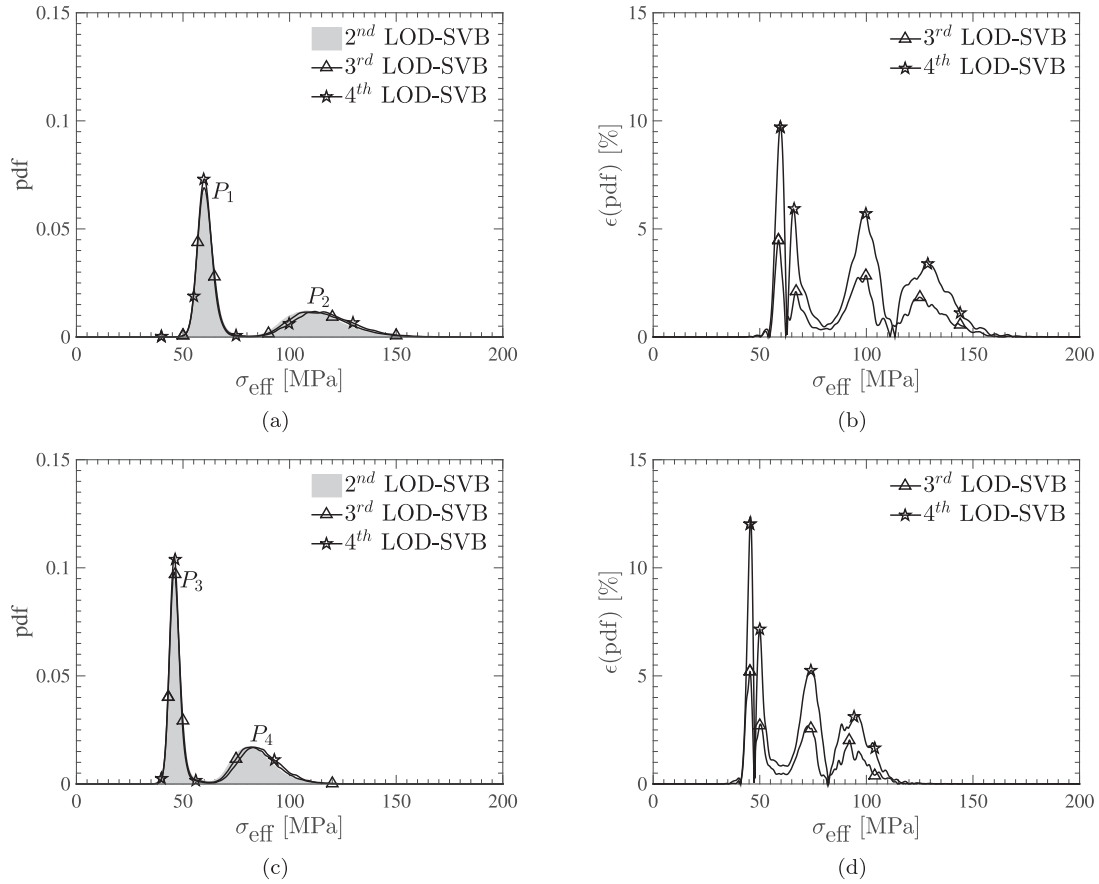

Fig. 12. Probability density functions of the effective stress σ_{eff} and the error of SVB microstructures. (a) Pdfs at the maximum stress. (b) Error at the maximum stress. (c) Pdfs at the end of relaxation. (d) Error at the end of relaxation.

distribution of the effective stress in each separate phase. Specifically, the left peak refers to the Al phase and the right peak identifies the Ni phase. This coincides with the observation, that the Ni phase carries higher stress than the Al phase at the same strain. Moreover, the translation of the pdf along the horizontal axis in Fig. 12c in comparison with Fig. 12a reflects the stress relaxation. The pdfs in Fig. 12a and c show a similar behavior of all SVB microstructures and their ability to capture the local stress fields at different loading points.

By comparing the pdf error between the 3rd and 4th LOD-SVB, we can see that the higher LOD-SVB introduces a larger error than the lower LOD-SVB, which is consistent with our previous analysis (see Fig. 12b and d). The error of the 4th LOD-SVB is limited within 12.34% and the 3rd LOD-SVB is below 5.20%.

To predict the error for pdfs associated with the 2nd LOD-SVB microstructure, we apply again RE on SVB microstructures at points P_1, P_2, P_3 and P_4 in Fig. 12. The computational value pdf^C, the extrapolated value pdf^E, and the extrapolated relative error $\epsilon(\text{pdf}^C)$ are listed in Table 4. The extrapolated relative error is defined as

$$\epsilon\left(\text{pdf}^C\right) = \frac{|\text{pdf}^E - \text{pdf}^C|}{|\text{pdf}^E|}. \tag{28}$$

The extrapolated relative error for all points is less than 7.3%, which indicates a very good convergence rate of the SVB computational results.

As a comparison, we show the pdfs of AVG and RND microstructures in Fig. 13a and c at time t_1 and t_2, respectively. The
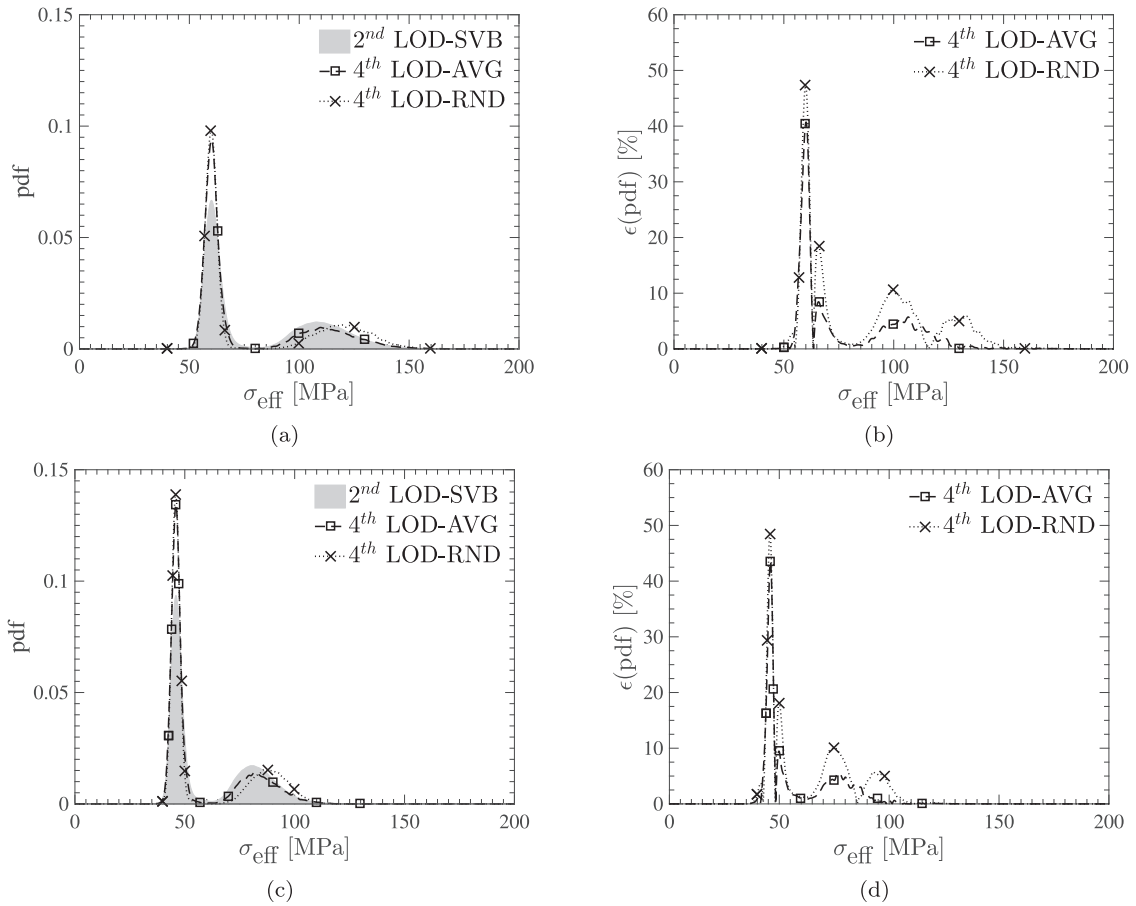
Fig. 13. Pdfs of the effective stress σ_{eff} of the 2nd LOD-SVB, AVG, and RND microstructures and the corresponding error. (a) Pdfs at the maximum stress. (b) Error at the maximum stress. (c) Pdfs at the end of relaxation. (d) Error at the end of relaxation.

Table 4
Richardson extrapoloation errors of the local stress at points, $P_1 - P_4$, in Fig. 12a and c.

RE point	pdf^C	pdf^E	$\epsilon(\text{pdf}^C)$
P_1	6.666e−2	6.330e−2	5.313e+0%
P_2	1.208e−2	1.209e−2	7.237e−2%
P_3	9.357e−2	9.004e−2	3.917e+0%
P_4	1.716e−2	1.810e−2	5.219e+0%

grey shaded area represents the pdf of the 2nd LOD-SVB. Again, the RND result is the average of five randomly generated microstructures. The coefficients of variation are CV(pdf) = 2.8% at t_1, and CV(pdf) = 3.0% at t_2. Although both AVG and RND microstructures are trying to capture the general shape of the stress distribution for both phases, we observe large errors. The AVG microstructure overshoots significantly at the peak of the Al phase and undershoots the peak of the Ni phase at both loading steps. As for the RND microstructure, it also overshoots at the peak of the Al phase. However, the peak of the Ni phase translates along the horizontal axis to the right, which means the RND microstructure predicts higher stress imposed on the Ni phase.

According to the error analysis in Fig. 13b and d, both AVG and RND microstructures produce the larger error at the peak of the Al phase. Moreover, the AVG microstructure generally exhibits smaller error than the RND microstructure. According to Fig. 13d, the AVG microstructure introduces a maximum 43.50% error and the RND introduces a maximum 48.77% error. In comparison with the corresponding error associated with the 4th LOD-SVB (12.34% error in

Fig. 12d), the AVG and RND microstructures produce much larger errors than SVB.

5.3. Mechanical response with random crystal orientation

In this subsection, we present the results of the mechanical response with random crystal orientations. Note that the reduction of the crystallographic orientations is also an active area of research. In this work, we simply assign a random texture to each LOD. Specifically, the 2nd, 3rd and 4th LOD-SVB crystal orientations are randomly generated for each finite element (i.e., a crystal). However, the 4th LOD-AVG has the same orientation as the 4th LOD-SVB for unbiased texture comparison. Five 4th LOD-RND microstructures each utilize one separately generated random texture.

The average Cauchy stress for all simulated microstructures is shown in Fig. 14a. The 4th LOD-RND result is the average of five different microstructures, with the coefficient of variation CV= 1.25%. The associated errors of the LODs are displayed in Fig. 14b. It is shown that the 3rd LOD-SVB produces the most accurate result. The 4th LOD-SVB introduces the least error among all of the 4th LOD microstructures, and the 4th LOD-AVG is the most erroneous.

In addition to the overall mechanical behavior, we also include the pdfs of the effective stress at time t_1 (maximum stress) in Fig. 15. We show the pdfs of the Al and Ni phases using darker and brighter grey, respectively. Again, the 4th LOD-RND distribution is the averaged result from five random microstructures. The coefficients of variation are CV(pdf) = 9.67% of the Al phase and
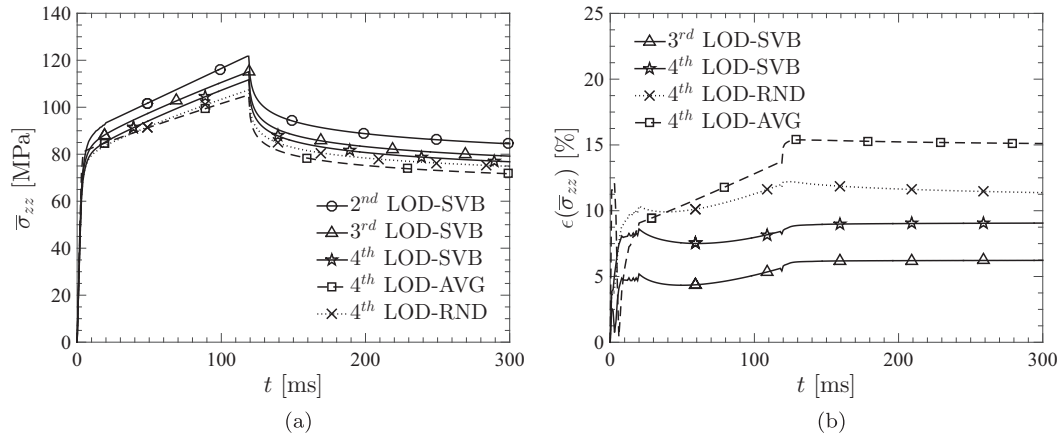
Fig. 14. The average normal stress of the 2nd − 4th LOD-SVB, AVG, and RND microstructures with the random crystal orientation. (a) Average normal stress versus time. (b) Error of the 3rd − 4th LOD microstructures.
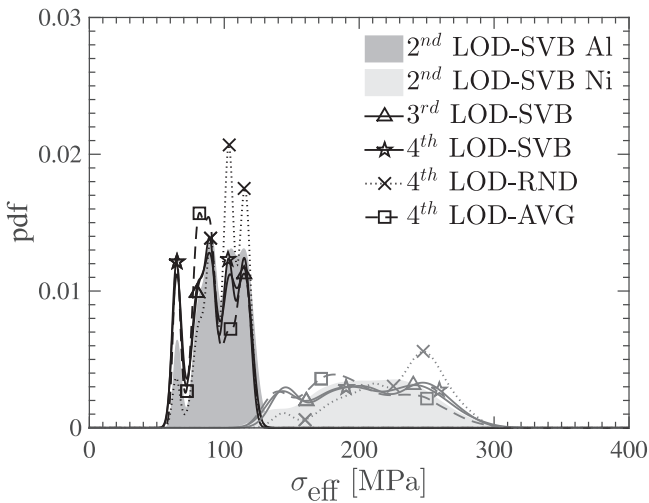

Fig. 15. Pdfs of the effective stress σ_{eff} for the 2nd − 4th LOD-SVB, AVG and RND microstructures with random crystal orientations.

tion. This highlights the coupling between the microstucture and the crystallographic orientations.

The associated pdf errors for both phases are shown in Fig. 16. The 3rd LOD-SVB is again the most accurate. The 4th LOD-RND is the most erroneous. The characteristics of the 4th LOD-SVB are close to that of the 3rd LOD-SVB. This indicates the consistency in the LOD-SVBs, and the convergence to the 2nd LOD-SVB (the finest microstructure used in this work). The 4th LOD-SVB has the maximum pdf error close to that of the 4th LOD-AVG. However, the 4th LOD-AVG does not converge to the 3rd LOD-SVB and attains the largest error around $\sigma_{\text{eff}} = 80$MPa. Moreover, the integral error of the 4th LOD-SVB is smaller than that of the 4th LOD-AVG (i.e., the L^2-norm error normalized with the 2nd LOD-SVB pdf is 28.47% for the 4th LOD-SVB versus 36.92% for the 4th LOD-AVG). The general increase of the pdf error (compared to Figs. 12b and 13d) indicates that the texture mapping is crucial for the mechanical behavior assessment of polycrystals. Thus, the initial texture reduction is important and has to be considered together with the reduction of the initial morphology.

6. Conclusion

We propose a novel image-based modeling technique with high-fidelity and a reduced amount of data for the analysis of complex heterogeneous materials. The SVB technique is based on VB – a Google Earth like method – that utilizes image compression while retaining important morphological features.
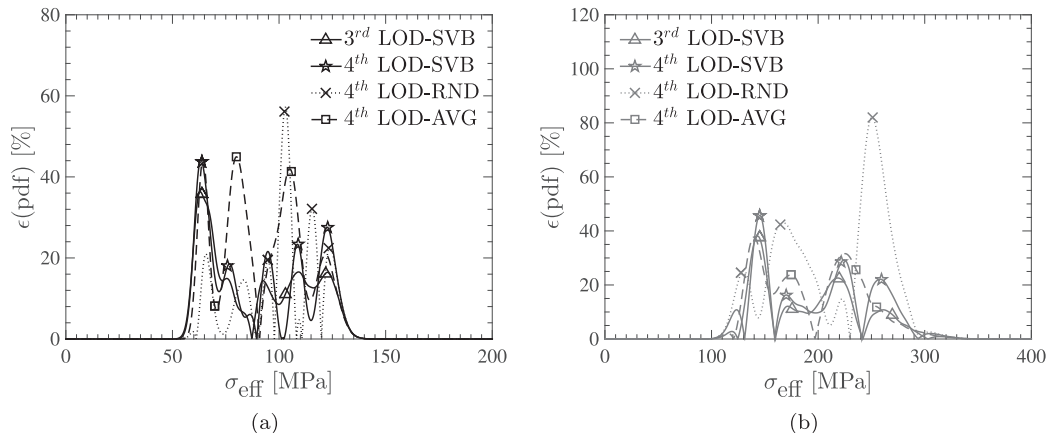
CV(pdf) = 14.91% of the Ni phase. This high CV(pdf) of the 4th LOD-RND shows the high sensitivity of the microstructural data (both texture and morphology).

Comparing Fig. 12a with Fig. 15, we observe the complex stress pdf for the case of random texture. The random crystal orientation creates multiple stress peaks and broadens the stress distribu-

Fig. 16. Pdf errors of the effective stress σ_{eff} for the 3rd − 4th LOD-SVB, the AVG and RND microstructures with random crystal orientations. (a) Phase Al. (b) Phase Ni.

We improve VB through minimizing density-like greyscale value PMFs among microstructure LODs. In particular, we design a filter to reconstruct the statistical properties of higher LODs in order to create a series of SVB microstructures. The material density indicator – the greyscale value PMF – is restored through this procedure.

According to the statistical characterization, the new SVB method preserves the one- and two-point correlation functions among all analyzed LODs. The statistical and mechanical behavior of SVB microstructures have the potential to efficiently reduce the computational complexity by performing computations on a coarser microstructure instead of on the finest one, while retaining a high-degree of accuracy.

We simulate a tension-relaxation loading process of HEBM Ni/Al composites assuming both a single crystal representation and random textures. We study macro- and micro-mechanical responses using the overall and local stress fields, respectively. Error analysis shows promise of the SVB microstructures in capturing the mechanical behavior. RE confirms the convergence properties of the SVB technique. An analysis of a polycrystal with random texture shows the importance of the crystallography and the need for a proper orientation reduction.

This novel SVB model can be applied to a variety of material systems. It lends itself to data compression and computational analysis with controlled accuracy in computational materials science studies.

Acknowledgement

References

Allaoui, A., Bai, S., Cheng, H.-M., Bai, J., 2002. Mechanical and electrical properties of a mwnt/epoxy composite. Compos. Sci. Technol. 62 (15), 1993–1998.

Arns, C.H., Knackstedt, M.A., Pinczewski, W.V., Garboczi, E.J., 2002. Computation of linear elastic properties from microtomographic images: methodology and agreement between theory and experiment. Geophysics 67 (5), 1396–1405.

Behrendt, S., Colditz, C., Franzke, O., Kopf, J., Deussen, O., 2005. Realistic real-time rendering of landscapes using billboard clouds. In: Computer Graphics Forum, vol. 24. Wiley Online Library, pp. 507–516.

Beran, M.J., Pytte, A., 1968. Statistical continuum theories. Am. J. Phys. 36 (10). 923–923.

Blavette, D., Bostel, A., Sarrau, J., Deconihout, B., Menand, A., 1993. An atom probe for three-dimensional tomography. Nature 363 (6428), 432–435.

Böhm, H.J., Eckschlager, A., Han, W., 2002. Multi-inclusion unit cell models for metal matrix composites with randomly oriented discontinuous reinforcements. Comput. Mater. Sci 25 (1), 42–53.

Bozek, J., Hochhalter, J., Veilleux, M., Liu, M., Heber, G., Sintay, S., Rollett, A., Littlewood, D., Maniatty, A., Weiland, H., et al., 2008. A geometric approach to modeling microstructurally small fatigue crack formation: i. probabilistic simulation of constituent particle cracking in aa 7075-t651. Modell. Simul. Mater. Sci. Eng. 16 (6), 065007.

Chawla, N., Sidhu, R., Ganesh, V., 2006. Three-dimensional visualization and microstructure-based modeling of deformation in particle-reinforced composites. Acta Mater. 54 (6), 1541–1548.

Choi, Y.S., Groeber, M.A., Shade, P.A., Turner, T.J., Schuren, J.C., Dimiduk, D.M., Uchic, M.D., Rollett, A.D., 2014. Crystal plasticity finite element method simulations for a polycrystalline ni micro-specimen deformed in tension. Metal. Mater. Trans. A 45 (13), 6352–6359.

Collins, B., Maggi, F., Matous, K., Jackson, T., Buckmaster, J., 2008. Using tomography to characterize heterogeneous propellants. AIAA Paper 941, 2008.

Decaudin, P., Neyret, F., 2004. Rendering forest scenes in real-time. In: EGSR04: 15th Eurographics Symposium on Rendering. Eurographics Association, pp. 93–102.

Decaudin, P., Neyret, F., 2009. Volumetric billboards. In: Computer Graphics Forum, vol. 28. Wiley Online Library, pp. 2079–2089.

Décoret, X., Durand, F., Sillion, F.X., Dorsey, J., 2003. Billboard clouds for extreme model simplification. In: ACM Transactions on Graphics (TOG), 22. ACM, pp. 689–696.

Drummond, J.L., De Carlo, F., Super, B.J., 2005. Three-dimensional tomography of composite fracture surfaces. J. Biomed. Mater. Res. Part B 74 (2), 669–675.

Fecht, H., Hellstern, E., Fu, Z., Johnson, W., 1990. Nanocrystalline metals prepared by high-energy ball milling. Metall. Trans. A 21 (9), 2333–2337.

Frank, J., 1992. Electron Tomography. Springer.

Fu, S.-Y., Feng, X.-Q., Lauke, B., Mai, Y.-W., 2008. Effects of particle size, particle/matrix interface adhesion and particle loading on mechanical properties of particulate–polymer composites. Compos. Part B 39 (6), 933–961.

Gerstl, S.S., Seidman, D.N., Gribb, A.A., Kelly, T.F., 2004. Leap microscopes look at tial alloys. Adv. Mater. Processes 162 (10), 31–33.

Gillman, A., Amadio, G., Matouš, K., Jackson, T., 2015. Third-order thermo-mechanical properties for packs of platonic solids using statistical micromechanics. In: Proc. R. Soc. A, vol. 471. The Royal Society, p. 20150060.

Gillman, A., Matouš, K., 2014. Third-order model of thermal conductivity for random polydisperse particulate materials using well-resolved statistical descriptions from tomography. Phys. Lett. A 378 (41), 3070–3073.

Gillman, A., Matouš, K., Atkinson, S., 2013. Microstructure-statistics-property relations of anisotropic polydisperse particulate composites using tomography. Phys. Rev. E 87 (2), 022208.

Goswami, P., Erol, F., Mukhi, R., Pajarola, R., Gobbetti, E., 2013. An efficient multi-resolution framework for high quality interactive rendering of massive point clouds using multi-way kd-trees. Vis. Comput. 29 (1), 69–83.

Gusev, A.A., 1997. Representative volume element size for elastic composites: a numerical study. J. Mech. Phys. Solids 45 (9), 1449–1459.

Hartl, D., Lagoudas, D.C., 2008. Thermomechanical characterization of shape memory materials. In: Shape Memory Alloys. Springer, pp. 53–119.

Heckbert, P., Garland, M., 1994. Multiresolution modeling for fast rendering. Graphics Interface. Canadian Information Processing Society. 43–43.

Huang, M., Li, Y.-m., 2013. X-Ray tomography image-based reconstruction of microstructural finite element mesh models for heterogeneous materials. Comput. Mater. Sci 67, 63–72.

Huang, Y., Yang, Z., Ren, W., Liu, G., Zhang, C., 2015. 3D meso-scale fracture modelling and validation of concrete based on in-situ x-ray computed tomography images using damage plasticity model. Int. J. Solids Struct. 67, 340–352.

Jain, A.K., 1989. Fundamentals of Digital Image Processing. Prentice-Hall, Inc.

Klemm, A., Müller, H.-P., Kimmich, R., 1997. Nmr microscopy of pore-space backbones in rock, sponge, and sand in comparison with random percolation model objects. Phys. Rev. E 55 (4), 4413.

Kulkarni, M.G., Geubelle, P.H., Matouš, K., 2009. Multi-scale modeling of heterogeneous adhesives: effect of particle decohesion. Mech. Mater. 41 (5), 573–583.

Kumar, H., Briant, C., Curtin, W., 2006. Using microstructure reconstruction to model mechanical behavior in complex microstructures. Mech. Mater. 38 (8), 818–832.

Kumar, N.C., Matouš, K., Geubelle, P.H., 2008. Reconstruction of periodic unit cells of multimodal random particulate composites using genetic algorithms. Comput. Mater. Sci 42 (2), 352–367.

Larson, B., Yang, W., Ice, G., Budai, J., Tischler, J., 2002. Three-dimensional x-ray structural microscopy with submicrometre resolution. Nature 415 (6874), 887–890.

Lee, H., Brandyberry, M., Tudor, A., Matouš, K., 2009. Three-dimensional reconstruction of statistically optimal unit cells of polydisperse particulate composites from microtomography. Phys. Rev. E 80 (6), 061301.

Lee, H., Gillman, A.S., Matouš, K., 2011. Computing overall elastic constants of polydisperse particulate composites from microtomographic data. J. Mech. Phys. Solids 59 (9), 1838–1857.

Lewis, A., Geltmacher, A., 2006. Image-based modeling of the response of experimental 3d microstructures to mechanical loading. Scr. Mater. 55 (1), 81–85.

Lin, W., Dong, L., 2006. Adaptive downsampling to improve image compression at low bit rates. IEEE Trans. Image Process. 15 (9), 2513–2521.

Lindstrom, P., Koller, D., Ribarsky, W., Hodges, L.F., Faust, N., Turner, G.A., 1996. Real-time, continuous level of detail rendering of height fields. In: Proceedings of the 23rd Annual Conference on Computer Graphics and Interactive Techniques. ACM, pp. 109–118.

Lorensen, W.E., Cline, H.E., 1987. Marching cubes: a high resolution 3d surface construction algorithm. In: ACM siggraph computer graphics, vol. 21. ACM, pp. 163–169.

Luebke, D.P., 2003. Level of Detail for 3D Graphics. Morgan Kaufmann.

Mammen, A., 1989. Transparency and antialiasing algorithms implemented with the virtual pixel maps technique. IEEE Comput. Graph. Appl. 9 (4), 43–55.

Man, H.-K., van Mier, J.G., 2008. Influence of particle density on 3d size effects in the fracture of (numerical) concrete. Mech. Mater. 40 (6), 470–486.

Manukyan, K.V., Shuck, C.E., Rogachev, A.S., Mukasyan, A.S., 2015. Preparation and reactivity of gasless nanostructured energetic materials. JoVE (J. Vis. Exp.). e52624–e52624.

Matouš, K., Geers, M.G., Kouznetsova, V.G., Gillman, A., 2017. A review of predictive nonlinear theories for multiscale modeling of heterogeneous materials. J. Comput. Phys. 330, 192–220.

Matouš, K., Kulkarni, M.G., Geubelle, P.H., 2008. Multiscale cohesive failure modeling of heterogeneous adhesives. J. Mech. Phys. Solids 56 (4), 1511–1533.

Matouš, K., Lepš, M., Zeman, J., Šejnoha, M., 2000. Applying genetic algorithms to selected topics commonly encountered in engineering practice. Comput. Methods Appl. Mech. Eng. 190 (13), 1629–1650.

Matouš, K., Maniatty, A.M., 2004. Finite element formulation for modelling large deformations in elasto-viscoplastic polycrystals. Int. J. Numer. Methods Eng. 60 (14), 2313–2333.

Matouš, K., Maniatty, A.M., 2009. Multiscale modeling of elasto-viscoplastic polycrystals subjected to finite deformations. Interaction and multiscale mechanics 2, 375–396.

Meyers, M.A., Mishra, A., Benson, D.J., 2006. Mechanical properties of nanocrystalline materials. Prog. Mater. Sci. 51 (4), 427–556.

Midgley, P., Weyland, M., 2003. 3D electron microscopy in the physical sciences: the development of z-contrast and eftem tomography. Ultramicroscopy 96 (3), 413–431.

Montal, M., Mueller, P., 1972. Formation of bimolecular membranes from lipid monolayers and a study of their electrical properties. Proc. Nation. Acad. Sci. 69 (12), 3561–3566.

Mosby, M., Matouš, K., 2015a. Hierarchically parallel coupled finite strain multiscale solver for modeling heterogeneous layers. Int. J. Numer. Methods Eng. 102 (3–4), 748–765.

Mosby, M., Matouš, K., 2015b. On mechanics and material length scales of failure in heterogeneous interfaces using a finite strain high performance solver. Modell. Simul. Mater. Sci. Eng. 23 (8), 085014.

Mosby, M., Matouš, K., 2016. Computational homogenization at extreme scales. Extreme Mech. Lett. 6, 68–74.

Otsu, N., 1975. A threshold selection method from gray-level histograms. Automatica 11 (285–296), 23–27.

Porter, T., Duff, T., 1984. Compositing digital images. In: ACM Siggraph Computer Graphics, vol. 18. ACM, pp. 253–259.

Povirk, G., 1995. Incorporation of microstructural information into models of two-phase materials. Acta Metall. Mater. 43 (8), 3199–3206.

Pyle, D.M., Lu, J., Littlewood, D.J., Maniatty, A.M., 2013. Effect of 3d grain structure representation in polycrystal simulations. Comput. Mech. 52 (1), 135–150.

Qidwai, M.S., Lewis, A.C., Geltmacher, A.B., 2009. Using image-based computational modeling to study microstructure–yield correlations in metals. Acta Mater. 57 (14), 4233–4247.

Richardson, L.F., 1911. The approximate arithmetical solution by finite differences of physical problems involving differential equations, with an application to the stresses in a masonry dam. In: Philosophical Transactions of the Royal Society of London. Series A, Containing Papers of a Mathematical or Physical Character, 210, pp. 307–357.

Richardson, L.F., Gaunt, J.A., 1927. The deferred approach to the limit. part i. single lattice. part ii. interpenetrating lattices. In: Philosophical Transactions of the Royal Society of London. Series A, Containing Papers of a Mathematical or Physical Character, 226, pp. 299–361.

Rodríguez, M.B., Gobbetti, E., Marton, F., Tinti, A., 2013. Compression-domain seamless multiresolution visualization of gigantic triangle meshes on mobile devices. In: Proceedings of the 18th International Conference on 3D Web Technology. ACM, pp. 99–107.

Russ, J.C., Woods, R.P., 1995. The image processing handbook. J. Comput. Assist. Tomogr. 19 (6), 979–981.

Schmidt, S., Nielsen, S.F., Gundlach, C., Margulies, L., Huang, X., Jensen, D.J., 2004. Watching the growth of bulk grains during recrystallization of deformed metals. Science 305 (5681), 229–232.

Seto, J.Y., 1975. The electrical properties of polycrystalline silicon films. J. Appl. Phys. 46 (12), 5247–5254.

Shuck, C.E., Frazee, M., Gillman, A., Beason, M.T., Gunduz, I.E., Matouš, K., Winarski, R., Mukasyan, A., 2016. X-Ray nanotomography and focused-ion-beam sectioning for quantitative three-dimensional analysis of nanocomposites. J. Synchrotron. Radiat. 23 (4).

Song, S.H., Paulino, G.H., Buttlar, W.G., 2006. Simulation of crack propagation in asphalt concrete using an intrinsic cohesive zone model. J. Eng. Mech. 132 (11), 1215–1223.

Srinivasan, K., Matouš, K., Geubelle, P.H., Jackson, T., 2009. Thermomechanical modeling of regressing heterogeneous solid propellants. J. Comput. Phys. 228 (21), 7883–7901.

Tanner, C.C., Migdal, C.J., Jones, M.T., 1998. The clipmap: a virtual mipmap. In: Proceedings of the 25th Annual Conference on Computer Graphics and Interactive Techniques. ACM, pp. 151–158.

Torquato, S., 2002. Statistical description of microstructures. Annu. Rev. Mater. Res. 32 (1), 77–111.

Torquato, S., 2013. Random heterogeneous materials: Microstructure and macroscopic properties, vol. 16. Springer Science & Business Media.

Turner, T., Shade, P., Schuren, J., Groeber, M., 2012. The influence of microstructure on surface strain distributions in a nickel micro-tension specimen. Modell. Simul. Mater. Sci. Eng. 21 (1), 015002.

Uchic, M.D., Groeber, M.A., Dimiduk, D.M., Simmons, J., 2006. 3D microstructural characterization of nickel superalloys via serial-sectioning using a dual beam fib-sem. Scr. Mater. 55 (1), 23–28.

Williams, L., 1983. Pyramidal parametrics. In: ACM Siggraph Computer Graphics, vol. 17. ACM, pp. 1–11.

Yeong, C., Torquato, S., 1998a. Reconstructing random media. Phys. Rev. E 57 (1), 495.

Yeong, C., Torquato, S., 1998b. Reconstructing random media. Phys. Rev. E 57 (1), 495.

Zhang, D., 2004. Processing of advanced materials using high-energy mechanical milling. Prog. Mater. Sci. 49 (3), 537–560.